Aerospace Science and Technology 155 (2024) 109652

Contents lists available at ScienceDirect

Aerospace Science and Technology

journal homepage: www.elsevier.com/locate/aescte

Aero-thermodynamic responses of a novel FGM sector disks using mathematical modeling and deep neural networks

Shaoyong Han [a,b], Zhen Wang [c,d,*], Mohammed El-Meligy [e,f], Kashif Saleem [g]

[a] School of Mathematics and Computer Science, Tongling University, Tongling, Anhui 244061, China
[b] Anhui Tongguan Intelligent Technology Co., Ltd., Tongling, Anhui 244000, China
[c] School of Data Science and Artificial Intelligence, Wenzhou University of Technology, Wenzhou, Zhejiang 325035, China
[d] Faculty of Computing, Universiti Teknologi Malaysia, Johor Bahru, Johor 81310, Malaysia
[e] Jadara University Research Center, Jadara University, PO Box 733, Irbid, Jordan
[f] Applied Science Research Center, Applied Science Private University, Amman, Jordan
[g] Department of Computer Science & Engineering, College of Applied Studies & Community Service, King Saud University, Riyadh, 11362, Saudi Arabia

ARTICLE INFO

Keywords:
Aerodynamic
Thermodynamic
Deep neural networks technique
Functionally graded material
Composite sector disks

ABSTRACT

Composite sector disks have extensive applications in aerospace industries, particularly when exposed to challenging conditions such as supersonic airflow and thermal environments. These applications leverage the superior properties of composite materials, including high strength-to-weight ratios, enhanced durability, and excellent thermal resistance, to meet the stringent requirements of aerospace operations. Multi-directional functionally graded (MD-FG) materials due to high-temperature resistance and other amazing properties in each direction have gotten plenty of attention recently. So, in this research, a thermoelasticity solution has been presented to study fundamental frequency traits of an MD-FG sector disk in supersonic airflow via both mathematics simulation and deep neural networks technique. For obtaining exact displacement fields, along with defining the changes of transverse shear strains along the system's thickness, the refined zigzag hypothesis is utilized. For obtaining the temperature-dependent equations, heat conduction relation and thermal boundary conditions of the MD-FG structure are presented. A coupled quasi-3D new refined theory (Q3D-NRT) and generalized differential quadrature method (GDQM) are presented for obtaining and solving the partial differential equations in the time-displacement domain. After obtaining the mathematics results, appropriate datasets are made for testing, training, and validation of the deep neural networks technique. Finally, the results have shown that aerodynamic pressure, temperature changes, Mach number, free stream speed, and air yaw angle have a major role in the stability/instability analyses of the thermally affected MD-FG sector disk in supersonic airflow. As an amazing outcome, increasing the sector angle, FG indexes, and temperature change lead to the reduction of the critical Mach number, and aerodynamic pressure associated with the flutter phenomenon.

1. Introduction

Composite materials are widely utilized in diverse engineering targets thanks to numerous merits such as high strength (or stiffness). As composite structures continue to evolve, advancements in material science are leading to even more specialized applications [1,2]. For instance, hybrid composites, which combine two or more types of reinforcements, offer improved properties over single-reinforcement composites, providing engineers with greater flexibility in material design [3]. These materials are being used in high-performance sports equipment, advanced medical devices, and even civil engineering structures, such as bridges and buildings, where durability and reduced weight are critical [4]. One significant area of research is the development of smart composites, which integrate sensors and actuators within the material [5]. These embedded technologies can monitor the health of the structure in real-time, detecting damage or stress before failure occurs, making them invaluable for safety-critical applications like aircraft and spacecraft [6]. Manufacturing processes for composite structures have also advanced [7-9]. Techniques such as automated fiber placement and additive manufacturing (3D printing) enable precise control over the material layup, allowing for highly optimized and customized components [10]. These methods reduce material waste and improve production efficiency [11,12]. The challenges of composite

* Corresponding author.
E-mail address: wangzhen@wzu.edu.cn (Z. Wang).

https://doi.org/10.1016/j.ast.2024.109652
Received 11 July 2024; Received in revised form 24 September 2024; Accepted 3 October 2024
Available online 4 October 2024

Nomenclature

n_r, n_θ, and n_z the FG indexes in the r-, θ-, and z- directions
$()_c$ and $()_m$ the ceramic and metal phase
$E(r,\theta,z,T)$, $\alpha(r,\theta,z,T)$, $\rho(r,\theta,z,T)$, $G(r,\theta,z,T)$, $K(r,\theta,z,T)$, and $\nu(r,\theta,z,T)$ Young's modulus, thermal expansion, mass density, shear modulus, thermal conductivity, and Poisson's ratio, respectively
h, R_o, I, and β thickness, radius, moment inertia, and span angle, of disks, respectively
$\mathscr{u}$, $\mathscr{v}$, and $\mathscr{w}$ displacement fields of a certain point in the plate domain in the (r, θ, z) system.
$\mathscr{u}_0$, $\mathscr{v}_0$, and $\mathscr{w}_0$ displacement components of the mid-plane
$\mathscr{f}_r$, $\mathscr{f}_\theta$, and $\mathscr{w}_1$ rotations about the θ, r, and z axes, respectively
$\mathscr{w}_2$, and $\mathscr{w}_3$ The higher-order terms in the Taylor's series expansion.
ε_{kk}, and σ_{kk} $(k = r,\ \theta,\ z)$ normal stresses and strains in the main directions
$(\gamma_{\theta z}, \gamma_{rz}, \gamma_{r\theta})$, and $(\tau_{\theta z}, \tau_{rz}, \tau_{r\theta})$ shear strain and stress
c_h, and R_h The system's specific heat and heat generation in the system
Λ_k, Λ_e, and $\Lambda_{\mathscr{w}}$ Kinetic and potential energies, as well as work done by the system
Λ_1, and Λ_2 external works due to the airflow
(T, T_1, T_2), and ∇ temperature gradient, and Laplace operator
ΔP aerodynamic pressure loading at high supersonic speeds
M_∞, λ_∞, θ_∞, and U_∞ Mach number, aerodynamic pressure, air yaw angle, and free stream speed
$\mathscr{M}$, $\mathscr{K}$, and $\mathscr{C}$ mass, stiffness, and damping of the system
$\aleph$, d, and b displacement vector, domain nodal points, and boundary nodal-points
ω, and $\overline{\varpi}$ dimensional natural frequency and its non-dimensional form
S, C, and F represent simply, clamped, and free supported boundary conditions, respectively

recycling are being addressed as well [13,14]. With an increased focus on sustainability, innovations in chemical recycling methods aim to recover valuable fibers and resins, making composite materials more eco-friendly [15]. Despite these advancements, the adoption of composites in some industries is still limited by high upfront costs and the need for specialized fabrication techniques [16]. However, as manufacturing processes become more efficient and material costs decrease, composite structures are expected to play an even larger role in the future of engineering [17]. Their ability to provide tailored solutions to complex engineering problems ensures that composites will remain a vital area of material science and engineering innovation for years to come [18].

However, drawbacks, such as sharp variation of stresses from one layer to another or inability to endure the higher values of thermal loads [19] bring about a novel sort of semi-composite materials so-called functionally graded materials (FGMs). Due to their superior usage in diverse engineering objectives, mechanical characteristics of FG structures, especially in one direction, have been scrutinized by many scholars [20-22].

Stability analysis of structures is a critical aspect of engineering, ensuring that structures can withstand applied loads without experiencing failure due to instability, such as buckling or collapse [23]. Engineers must assess stability to guarantee the safety and functionality of buildings, bridges, towers, and other load-bearing structures [24]. Without proper stability analysis, even a well-designed structure might fail under certain conditions, potentially leading to catastrophic consequences [25,26].

Mathematical modeling of structures is a fundamental tool for engineers to predict the behavior of physical systems under various conditions [27]. It allows for the analysis of stress, strain, and deformation in complex structures, helping to ensure safety and performance [28]. By simulating different scenarios, engineers can optimize designs to meet specific requirements while minimizing material costs and weight [29]. Accurate models help to reduce the need for extensive physical prototyping, thus saving time and resources [30]. Mathematical models also provide insight into failure mechanisms, allowing engineers to design structures with higher reliability [31]. In fields like aerospace, civil, and mechanical engineering, modeling is essential for understanding dynamic loading, vibration, and fatigue [32]. The use of models ensures compliance with safety standards and regulations, which is critical in many engineering applications [33]. It also supports engineers in conducting sensitivity analyses and identifying the most influential parameters affecting a structure's performance [34].

Based on an investigation by Steinberg [35], the aerospace craft's fuselage withstands an exceedingly high thermal load with extreme temperature gradient, especially when that reaches an altitude and speed of 29 km and Mach 8. In this situation, the common one-directional FG materials are improper to tolerate far more violent temperature changes. To overcome this defect, multi-directional FG (MD-FG) materials, with the ability to resist high-temperature fields, are introduced [36]. Accordingly, it is worth mentioning some studies in which structure is made of MD-FG materials. Nonlinear dynamical characteristics of a three-layer sandwich plate made of two-directional FG (2D-FG) porous materials, supported by an elastic medium, and subjected to a moving load were explored by Esmaeilzadeh et al. [37]. Allahkarami et al. [38] studied the influence of various parameters such as boundary types, thickness-to-radius ratio, porosity coefficient associated with even and uneven distribution types, FG (or power-law) index, and medium constants on the stability/instability characteristics of an MD-FG porous cylindrical shell. In those papers, the third-order shear deformation hypothesis, and generalized differential quadrature (GDQ) in addition to Bolotin's methods were used to model the structure and extract the stable regions, respectively. In another paper, the first-order shear deformation hypothesis in conjunction with geometrical nonlinearity, and the Galerkin method along with the multiple scale method were utilized for mathematical modeling and analysis of the nonlinear dynamic response of in-Plane 2D-FG Rectangular Plate whose material properties affected by temperature changes [39]. They showed that FG indexes have a major role in the nonlinear traits of the structure. Also, the vibrational behavior of a temperature-dependent FG disk with 2D temperature and material distributions was probed by Saini et al. [40].

The structure's unstable vibrational behavior or flutter phenomenon, which is due to the aerodynamic forces, can cause noticeable deformations and fatigue in the systems in addition to lessening the structure's life. In the following, a brief review of the available papers on the flutter study of different structures under supersonic airflow has been carried out [41-43]. Upon the first-order piston and classical plate hypotheses together regarding the aerodynamic damping and magnetorheological fluid, the flutter behavior of a sandwich plate was analyzed by Eshaghi [44]. Through the sensitivity analyses of the aerodynamic stiffness matrix, Song et al. [42] suggested a new approach for passive control of axially FG panels and beams under supersonic airflow. They derived the optimum Young's modulus as well as thickness functions and explained that the variation of the flutter modes leads to escalating the flutter bound. Upon the first-order shear deformation theory, Zhong et al. [45] studied the flutter boundaries of electromagnetic FG porous plates in a thermal environment and under supersonic airflow. They exhibited that reducing the FG indexes has a positive effect on the escalation of flutter bound. Also, the porosity factor and its pattern, together with boundary type have chief roles in the structure's critical aerodynamic pressure. Utilizing the Navier-solution, Lagrange processing, together with the first-order piston hypothesis, all relations corresponded to the flutter traits and vibrational behavior of FG cylindrical panels, which are constructed from open-cell metal foams and reinforced via graphene platelets, with porosity effect, and under supersonic flow were analyzed by Zhou et al. [46]. Nonlinear flutter and buckling traits of an FG cylindrical shell reinforced with composite materials under supersonic airflow were probed by Asadi and Wang [47]. In this article, it was displayed that the aerodynamic pressure and FG pattern of carbon nanotubes in polymer matrix have a major role in the system's deformation shapes. Through the isogeometric approach, Khalafi and Fazilati [48] explored the role of crack traits, temperature, and flow direction on the flutter traits of an FG plate in which the mechanical properties of one is temperature dependent. They expressed that the escalation of the crack length has a weakening effect on the critical flutter pressure if the flow direction and crack orientation become aligned.

This article, in addition to providing a thermoelastic solution, examines the influences of supersonic airflow parameters, such as aerodynamic pressure, Mach number, air yaw angle, as well as free stream speed, together with aerodynamics, and FG indexes on the vibration frequency of MD-FG sector disk in the thermal environment are the main goals of this investigation. To factor in the change of shear strains along the system's thickness, a coupled Q3D-NRT upon the refined zigzag hypothesis has been utilized. Accordingly, this study endeavors to examine the vibrational traits of an innovative geometric structure called MD-FG sector disks. To this end, the GDQM is employed to solve resultant equations derived through Hamilton's principle. After obtaining the mathematics results, appropriate datasets are made for testing, training, and validation of the deep neural networks technique. Finally, the results show that aerodynamic pressure, temperature changes, Mach number, free stream speed, and air yaw angle have a chief role in the stability boundaries of the thermally affected MD-FG sector disk in supersonic airflow.

2. Effective material properties: MD-FG materials

The effective mechanical property $\wp$ of an MD-FG disk can be written as

$$\wp(r,\theta,z,T) = \wp_m + (\wp_c - \wp_m)\left(0.5+\frac{z}{h}\right)^{n_z}\left(\frac{r-R_i}{R_o-R_i}\right)^{n_r}\left(\frac{\theta}{\theta_m}\right)^{n_\theta}, \tag{1}$$

Effective Young's modulus, $E(r,\ \theta,\ z,\ T)$, thermal expansion coefficients, $\alpha(r,\theta,z,T)$, mass density $\rho(r,\theta,z,T)$, shear modulus, $G(r,\theta,z,T)$, thermal conductivity, $K(r,\theta,z,T)$, along with Poisson's ratio, $\vartheta(r,\theta,z,T)$, can be derived from the Eq. (1). Also, it is supposed that the mechanical property $\wp(r,\theta,z,T)$ is temperature-dependent [49]. So,

$$\wp = \wp_0\left(\wp_{-1}T^{-1} + \wp_1 T + \wp_2 T^2 + \wp_3 T^3 + 1\right). \tag{2}$$

The temperature-dependent coefficients in Eq. (2), i.e. $\wp_0$, $\wp_{-1}$, $\wp_1$, $\wp_2$ and $\wp_3$, are tabulated in Table 1. Since the mechanical properties of structure vary in various directions, the mid-plane is different from the neutral plane [50].

3. Mathematical modeling

The schematic of an MD-FG disk with its corresponding dimensions is shown in Fig. 1.

3.1. Displacement field

As stated before, a Q3D-NRT is hired to introduce the structure's kinematic field. Therefore,

$$u(r,\theta,z,t) = u_0(r,\theta,t) - \left(\frac{5z^3}{3h^2}-\frac{z}{4}\right)\frac{\partial w_0(r,\theta,t)}{\partial r} + \frac{5}{4}\left(z-\frac{4z^3}{3h^2}\right)\varphi_r(r,\theta,t), \tag{3}$$

$$v(r,\theta,z,t) = v_0(r,\theta,t) - \left(\frac{5z^3}{3h^2}-\frac{z}{4}\right)\frac{\partial w_0(r,\theta,t)}{r\partial\theta} + \frac{5}{4}\left(z-\frac{4z^3}{3h^2}\right)\varphi_\theta(r,\theta,t),$$

$$w(r,\theta,z,t) = w_0(r,\theta,t) + z w_1(r,\theta,t) + z^2 w_2(r,\theta,t) + z^3 w_3(r,\theta,t).$$

Table 1
The temperature-dependent material properties of the MD-FG disk [49].

$\wp$	$\wp_0$	$\wp_{-1}$	$\wp_1$	$\wp_2$	$\wp_3$
Ceramic (Al_2O_3)					
$E_c[pa]$	348.43×10^{9}	0	-3.070×10^{-4}	2.160×10^{-7}	-8.946×10^{-11}
$\alpha_c[K^{-1}]$	5.8723×10^{-6}	0	9.095×10^{-4}	0	0
$K_c[W.m^{-1}K^{-1}]$	13.723	0	-1.032×10^{-3}	5.466×10^{-7}	-7.876×10^{-11}
ϑ_c	0.2400	0	0	0	0
$\rho_c[Kg.m^{-3}]$	2370	0	0	0	0
Metal (SUS304)					
$E_m[pa]$	201.04×10^{9}	0	3.079×10^{-4}	-6.534×10^{-7}	0
$\alpha_m[K^{-1}]$	12.330×10^{-6}	0	8.086×10^{-4}	0	0
$K_m[W.m^{-1}K^{-1}]$	15.379	0	-1.264×10^{-3}	2.092×10^{-6}	-7.223×10^{-10}
ϑ_m	0.3262	0	-2.002×10^{-4}	3.797×10^{-7}	0
$\rho_m[Kg.m^{-3}]$	8166	0	0	0	0

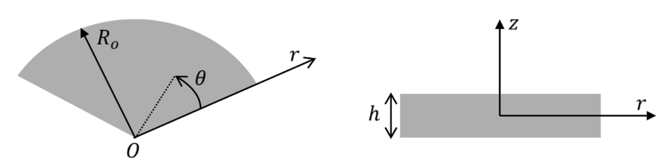

Fig. 1. Schematic of disk.

The strain-displacement relations are

$$\varepsilon_{rr} = \frac{\partial u}{\partial r},\ \varepsilon_{\theta\theta} = \frac{1}{r}\left(u + \frac{\partial v}{\partial \theta}\right),\ \varepsilon_{zz} = \frac{\partial w}{\partial z}, \tag{4}$$

$$\gamma_{r\theta} = \frac{1}{r}\frac{\partial u}{\partial \theta} + \frac{\partial v}{\partial r} - \frac{v}{r},\ \gamma_{rz} = \frac{\partial u}{\partial z} + \frac{\partial w}{\partial r},\ \gamma_{\theta z} = \frac{\partial v}{\partial z} + \frac{1}{r}\frac{\partial w}{\partial \theta}.$$

Next, the non-zero strain components are

$$\varepsilon_{rr} = \frac{\partial u_0}{\partial r} - C_1\frac{\partial^2 w_0}{\partial r^2} + C_2\frac{\partial u_1}{\partial r}, \tag{5a}$$

$$\varepsilon_{\theta\theta} = \frac{1}{r}\left(u_0 - C_1\frac{\partial w_0}{\partial r} + C_2 u_1 + \frac{\partial v_0}{\partial \theta} - \frac{C_1}{r}\frac{\partial^2 w_0}{\partial \theta^2} + C_2\frac{\partial v_1}{\partial \theta}\right), \tag{5b}$$

$$\varepsilon_{zz} = w_1 + 2z w_2 + 3z^2 w_3, \tag{5c}$$

$$\gamma_{rz} = -\frac{\partial C_1}{\partial z}\frac{\partial w_0}{\partial r} + \frac{\partial C_2}{\partial z}u_1 + \frac{\partial w_0}{\partial r} + z\frac{\partial w_1}{\partial r} + z^2\frac{\partial w_2}{\partial r} + z^3\frac{\partial w_3}{\partial r}, \tag{5d}$$

$$\gamma_{r\theta} = \frac{1}{r}\frac{\partial u_0}{\partial \theta} - \frac{C_1}{r}\frac{\partial^2 w_0}{\partial r\partial \theta} + \frac{C_2}{r}\frac{\partial u_1}{\partial \theta} + \frac{\partial v_0}{\partial r} - \frac{C_1}{r}\frac{\partial^2 w_0}{\partial r\partial \theta} + C_2\frac{\partial v_1}{\partial r} - \frac{v_0}{r} + \frac{2C_1}{r^2}\frac{\partial w_0}{\partial \theta} - \frac{C_2}{r}v_1, \tag{5e}$$

$$\gamma_{\theta z} = -\frac{1}{r}\frac{\partial C_1}{\partial z}\frac{\partial w_0}{\partial \theta} + \frac{\partial C_2}{\partial z}v_1 + \frac{1}{r}\frac{\partial w_0}{\partial \theta} + \frac{z}{r}\frac{\partial w_1}{\partial \theta} + \frac{z^2}{r}\frac{\partial w_2}{\partial \theta} + \frac{z^3}{r}\frac{\partial w_3}{\partial \theta}, \tag{5f}$$

where $C_1 = \frac{4z^3}{3h^2}$, and $C_2 = z - \frac{4z^3}{3h^2}$. Also, strain-stress relations considering the thermomechanical effects are

$$\begin{Bmatrix} \sigma_{rr} \\ \sigma_{\theta\theta} \\ \sigma_{zz} \\ \tau_{\theta z} \\ \tau_{rz} \\ \tau_{r\theta} \end{Bmatrix} = \begin{bmatrix} Q_{11} & Q_{12} & Q_{13} & 0 & 0 & 0 \\ Q_{21} & Q_{22} & Q_{23} & 0 & 0 & 0 \\ Q_{31} & Q_{32} & Q_{33} & 0 & 0 & 0 \\ 0 & 0 & 0 & Q_{44} & 0 & 0 \\ 0 & 0 & 0 & 0 & Q_{55} & 0 \\ 0 & 0 & 0 & 0 & 0 & Q_{66} \end{bmatrix} \begin{Bmatrix} \varepsilon_{rr} - \alpha\Delta T \\ \varepsilon_{\theta\theta} - \alpha\Delta T \\ \varepsilon_{zz} - \alpha\Delta T \\ \gamma_{\theta z} \\ \gamma_{rz} \\ \gamma_{r\theta} \end{Bmatrix}, \tag{6}$$

where

$$Q_{11} = 2Q_{44}\frac{(1 - \vartheta(r,\theta,z,T))}{(1 - 2\vartheta(r,\theta,z,T))}, Q_{33} = Q_{22} = Q_{11}, \tag{7}$$

$$Q_{12} = 2Q_{44}\frac{\vartheta(r,\theta,z,T)}{(1 - 2\vartheta(r,\theta,z,T))}, Q_{13} = Q_{23} = Q_{12},$$

$$Q_{44} = \frac{E(r,\theta,z,T)}{2(1 + \vartheta(r,\theta,z,T))}, Q_{66} = Q_{55} = Q_{44}.$$

Additionally, the heat conduction relation for the MD-FG conductive layer is [51]

$$\nabla^2 T + R_h = \rho c_h \frac{\partial T}{\partial t}. \tag{8}$$

It is worth expressing that the relation corresponding to steady state is derived by ignoring thermal generation. So,

$$\nabla^2 T = 0, \tag{9}$$

Finally, for the MD-FG conductive layer, we have

$$\begin{aligned} &\frac{1}{r}\frac{\partial}{\partial r}\left(rK(r,\theta,z,T)\frac{\partial T(r,\theta,z,T)}{\partial r}\right) + \frac{1}{r^2}\frac{\partial}{\partial\theta}\left(K(r,\theta,z,T)\frac{\partial T(r,\theta,z,T)}{\partial\theta}\right) \\ &+ \frac{\partial}{\partial z}\left(K(r,\theta,z,T)\frac{\partial T(r,\theta,z,T)}{\partial z}\right) \\ &= 0, \end{aligned} \tag{10}$$

whose thermal boundary conditions read as follows

$$T(R_i,\theta,z) = 0, T(r,0,z) = 0, T\left(r,\theta,-\frac{h}{2}\right) = T_1, \tag{11}$$

$$T(R_o,\theta,z) = 0, T(r,\theta_m,z) = 0, T\left(r,\theta,\frac{h}{2}\right) = T_2.$$

3.2. Hamilton's principle

The equilibrium equations in conjunction with boundary conditions are extracted by considering Hamilton's principle [52-54].

$$\int_{t_1}^{t_2} (\delta\Lambda_k - (\delta\Lambda_e - \delta\Lambda_w))dt = 0. \tag{12}$$

The kinetic, i.e. Λ_k, and potential, i.e. Λ_e, energies of the structure are

$$\Lambda_k = \int \rho\left[\left(\frac{\partial U}{\partial t}\right)^2 + \left(\frac{\partial V}{\partial t}\right)^2 + \left(\frac{\partial W}{\partial t}\right)^2\right]dV, \tag{13a}$$

$$\Lambda_e = \int \{\sigma_{zz}\varepsilon_{zz} + \sigma_{rr}\varepsilon_{rr} + \sigma_{\theta\theta}\varepsilon_{\theta\theta} + \tau_{r\theta}\gamma_{r\theta} + \tau_{\theta z}\gamma_{\theta z} + \tau_{rz}\gamma_{rz}\}dV. \tag{13b}$$

Also, the aerodynamic pressure, i.e. $\Delta P(r, \theta, t)$, which is a non-conservative force, leads to the generation of external work, i.e. Λ_w, on the system as:

$$\Lambda_w = \int_A \Delta P(r,\theta,t) w_0 dA, \tag{14}$$

Regarding Krumhaar's modified supersonic piston hypothesis together with the curvature effect, and utilizing the virtual work due to the aerodynamic load, i.e. ΔP, the aerodynamic stiffness matrix along with the aerodynamic damping matrix are obtained. So, at first, ΔP is

$$\begin{aligned} \Delta P = &-\frac{\rho U_\infty^2 M_\infty^2}{\sqrt{M_\infty^2 - 1}}\left(\frac{\partial w_0}{\partial r}\cos(\theta_\infty) + \frac{1}{r}\frac{\partial w_0}{\partial\theta}\sin(\theta_\infty)\right) \\ &-\frac{\rho U_\infty M_\infty (M_\infty^2 - 2)}{\sqrt{(M_\infty^2 - 1)^3}}\frac{\partial w_0}{\partial t}, \end{aligned} \tag{15}$$

Since $\lambda_\infty = \frac{\rho U_\infty^2}{\sqrt{M_\infty^2 - 1}}$, Eq. (15) can be written as:

$$\Delta P = -\lambda_\infty M_\infty^2\left(\frac{\partial w_0}{\partial r}\cos(\theta_\infty) + \frac{1}{r}\frac{\partial w_0}{\partial\theta}\sin(\theta_\infty)\right) - \lambda_\infty\frac{M_\infty (M_\infty^2 - 2)}{U_\infty (M_\infty^2 - 1)}\frac{\partial w_0}{\partial t}. \tag{16}$$

in which U_∞ shows the velocity of sound, and $M_\infty \geq 1.7$ is Mach number. To get the flutter relation of the supersonic disks, it is necessary to eliminate the stabilizer parameter, i.e. the aerodynamic damping term, from the aerodynamic load presented in Eq. (16).

Applying Eqs. (13a-b), and (14) into Eq. (12), leading to the following equations

$$\delta u_0 \quad : \quad \frac{1}{r}\frac{\partial(r\mathscr{N}_{rr})}{\partial r} - \frac{\mathscr{N}_{\theta\theta}}{r} + \frac{\partial\mathscr{N}_{r\theta}}{r\partial\theta} = I_0\frac{\partial^2 u_0}{\partial t^2} - K_0\frac{\partial^3 w_0}{\partial r\partial t^2} + K_1\frac{\partial^2 \varphi_r}{\partial t^2}, \tag{17a}$$

$$\delta v_0 \quad : \quad \frac{1}{r}\frac{\partial\mathscr{N}_{\theta\theta}}{\partial\theta} + \frac{1}{r}\frac{\partial(r\mathscr{N}_{r\theta})}{\partial r} + \frac{\mathscr{N}_{r\theta}}{r} = I_0\frac{\partial^2 v_0}{\partial t^2} - \frac{K_0}{r}\frac{\partial^3 w_0}{\partial\theta\partial t^2} + K_1\frac{\partial^2 v_0}{\partial t^2}, \tag{17b}$$

$$\delta w_0 \quad : \quad \begin{aligned} &\frac{\partial^2(r\mathscr{M}_{rr})}{\partial r^2} - \frac{\partial\mathscr{M}_{\theta\theta}}{\partial r} + \frac{1}{r}\frac{\partial^2\mathscr{M}_{\theta\theta}}{\partial\theta^2} - \frac{\partial(rR_{rz})}{\partial r} + \frac{\partial(r\mathscr{N}_{rz})}{\partial r} \\ &2\frac{\partial^2\mathscr{M}_{r\theta}}{\partial r\partial\theta} + 2\frac{\partial\mathscr{M}_{r\theta}}{\partial\theta} - \frac{\partial R_{\theta z}}{\partial\theta} + \frac{\partial\mathscr{N}_{\theta z}}{\partial\theta} + \Delta P = \frac{\partial}{\partial r}\left(rK_0\frac{\partial^2 u_0}{\partial t^2}\right) \\ &-\frac{\partial}{\partial r}\left(rL_0\frac{\partial^3 w_0}{\partial r\partial t^2}\right) + \frac{\partial}{\partial r}\left(rJ_0\frac{\partial^2\varphi_r}{\partial t^2}\right) + \frac{\partial}{\partial\theta}\left(K_0\frac{\partial^2 v_0}{\partial t^2}\right) \\ &-\frac{1}{r}\frac{\partial}{\partial\theta}\left(L_0\frac{\partial^3 w_0}{\partial\theta\partial t^2}\right) + \frac{\partial}{\partial\theta}\left(J_0\frac{\partial^3\varphi_\theta}{\partial t^2}\right) + rI_0\frac{\partial^2 w_0}{\partial t^2} + rI_1\frac{\partial^2 w_1}{\partial t^2} \\ &+rI_2\frac{\partial^2 w_2}{\partial t^2} + rI_3\frac{\partial^2 w_3}{\partial t^2} \end{aligned}, \tag{17c}$$

$$\delta\varphi_r \quad : \quad \frac{1}{r}\frac{\partial(r\mathscr{N}_{rr})}{\partial r} - \frac{\mathscr{N}_{\theta\theta}}{r} + \frac{\partial\mathscr{P}_{r\theta}}{\partial\theta} - \mathscr{S}_{rz} = K_1\frac{\partial^2 u_0}{\partial t^2} - J_0\frac{\partial^3 w_0}{\partial r\partial t^2} + L_1\frac{\partial^2\varphi_r}{\partial t^2}, \tag{17d}$$

$$\delta\varphi_\theta \quad : \quad \frac{\partial\mathscr{P}_{\theta\theta}}{\partial\theta} + \frac{\partial(r\mathscr{P}_{r\theta})}{\partial r} + \mathscr{P}_{r\theta} - r\mathscr{S}_{\theta z} = K_1 r\frac{\partial^2 v_0}{\partial t^2} - J_0\frac{\partial^3 w_0}{\partial\theta\partial t^2} + L_1 r\frac{\partial^2\varphi_\theta}{\partial t^2}, \tag{17e}$$

$$\delta w_1 \quad : \quad \frac{1}{r}\frac{\partial(r\mathscr{M}_{rz})}{\partial r} + \frac{1}{r}\frac{\partial\mathscr{M}_{\theta z}}{\partial\theta} - \mathscr{N}_{zz} = I_1\frac{\partial^2 w_0}{\partial t^2} + I_2\frac{\partial^2 w_1}{\partial t^2} + I_3\frac{\partial^2 w_2}{\partial t^2} + I_4\frac{\partial^2 w_3}{\partial t^2}, \tag{17f}$$

$$\delta w_2 \quad : \quad \frac{1}{r}\frac{\partial(r\mathscr{P}_{rz})}{\partial r} + \frac{1}{r}\frac{\partial\mathscr{P}_{\theta z}}{\partial\theta} - 2\mathscr{M}_{zz} = I_2\frac{\partial^2 w_0}{\partial t^2} + I_3\frac{\partial^2 w_1}{\partial t^2} + I_4\frac{\partial^2 w_2}{\partial t^2} + I_5\frac{\partial^2 w_3}{\partial t^2}, \tag{17 g}$$

$$\delta w_3 \quad : \quad \frac{1}{r}\frac{\partial(rQ_{rz})}{\partial r} + \frac{1}{r}\frac{\partial Q_{\theta z}}{\partial\theta} - 3\mathscr{P}_{zz} = I_3\frac{\partial^2 w_0}{\partial t^2} + I_4\frac{\partial^2 w_1}{\partial t^2} + I_5\frac{\partial^2 w_2}{\partial t^2} + I_6\frac{\partial^2 w_3}{\partial t^2}. \tag{17h}$$

In addition, the resultant boundary conditions can be written as

$$\delta u_0 = 0 \quad or \quad (r\mathscr{N}_{rr})\widehat{n}_r + (\mathscr{N}_{r\theta})\widehat{n}_\theta = 0, \tag{18a}$$

$$\delta v_0 = 0 \quad \text{or} \quad (r\mathscr{N}_{r\theta})\widehat{n}_r + (\mathscr{N}_{\theta\theta})\widehat{n}_\theta = 0, \tag{18b}$$

$$\delta w_0 = 0 \quad \text{or} \quad \left\{\frac{\partial(r\mathscr{M}_{rr})}{\partial r} - \mathscr{M}_{\theta\theta} - rR_{rz} + r\mathscr{N}_{rz}\right\}\widehat{n}_r + \left\{\frac{\partial\mathscr{M}_{\theta\theta}}{r\partial\theta} + \frac{2\partial\mathscr{M}_{r\theta}}{\partial r} + \frac{2\mathscr{M}_{r\theta}}{r} - R_{rz} + \mathscr{N}_{\theta z}\right\}\widehat{n}_\theta = 0, \tag{18c}$$

$$\delta \mathscr{V}_r = 0 \quad or \quad (r\mathscr{P}_{rr})\widehat{n}_r + (\mathscr{P}_{r\theta})\widehat{n}_\theta = 0, \tag{18d}$$

$$\delta \mathscr{V}_\theta = 0 \quad \text{or} \quad (r\mathscr{P}_{r\theta})\widehat{n}_r + (\mathscr{P}_{\theta\theta})\widehat{n}_\theta = 0, \tag{18e}$$

$$\delta w_1 = 0 \quad \text{or} \quad (r\mathscr{M}_{rz})\widehat{n}_r + (\mathscr{M}_{\theta z})\widehat{n}_\theta = 0, \tag{18f}$$

$$\delta w_2 = 0 \quad \text{or} \quad (r\mathscr{P}_{rz})\widehat{n}_r + (\mathscr{P}_{\theta z})\widehat{n}_\theta = 0, \tag{18 g}$$

$$\delta w_3 = 0 \quad \text{or} \quad (rQ_{rz})\widehat{n}_r + (Q_{\theta z})\widehat{n}_\theta = 0. \tag{18h}$$

where

$$\mathscr{N}_{rr} = \int_V (\sigma_{rr}) rdrd\theta dz,\ \mathscr{M}_{rr} = \int_V (C_1\sigma_{rr}) rdrd\theta dz,\ \mathscr{P}_{rr} = \int_V (C_2\sigma_{rr}) rdrd\theta dz, \tag{19}$$

$$\mathscr{N}_{\theta\theta} = \int_V (\sigma_{\theta\theta}) rdrd\theta dz,\ \mathscr{M}_{\theta\theta} = \int_V (C_1\sigma_{\theta\theta}) rdrd\theta dz,\ \mathscr{P}_{\theta\theta} = \int_V (C_2\sigma_{\theta\theta}) rdrd\theta dz,$$

$$\mathscr{N}_{zz} = \int_V (\sigma_{zz}) rdrd\theta dz,\ \mathscr{M}_{zz} = \int_V (z\sigma_{zz}) rdrd\theta dz,\ \ \mathscr{P}_{zz} = \int_V \left(z^2\sigma_{zz}\right) rdrd\theta dz,$$

$$\mathscr{N}_{\theta z} = \int_V (\tau_{\theta z}) rdrd\theta dz, \mathscr{M}_{\theta z} = \int_V (z\tau_{\theta z}) rdrd\theta dz,\ \ \mathscr{P}_{\theta z} = \int_V \left(z^2\tau_{\theta z}\right) rdrd\theta dz$$

$$Q_{\theta z} = \int_V \left(z^3\tau_{\theta z}\right) rdrd\theta dz,\ \mathscr{N}_{rz} = \int_V (\tau_{rz}) rdrd\theta dz, \mathscr{M}_{rz} = \int_V (z\tau_{rz}) rdrd\theta dz,$$

$$\mathscr{P}_{rz} = \int_V \left(z^2\tau_{rz}\right) rdrd\theta dz, Q_{rz} = \int_V \left(z^3\tau_{rz}\right) rdrd\theta dz,\ R_{rz} = \int_V \left(\frac{\partial C_1}{\partial z}\tau_{rz}\right) rdrd\theta dz$$

$$\mathscr{S}_{rz} = \int_V \left(\frac{\partial C_2}{\partial z}\tau_{rz}\right) rdrd\theta dz,\ \mathscr{N}_{r\theta} = \int_V (\tau_{r\theta}) rdrd\theta dz, \mathscr{M}_{r\theta} = \int_V (C_1\tau_{r\theta}) rdrd\theta dz,$$

$$\mathscr{P}_{r\theta} = \int_V (C_2\tau_{r\theta}) rdrd\theta dz,$$

$$I_j = \int_r\int_\theta\int_z \rho(r,\theta,z) r z^j dz d\theta dr \text{in which } j = 0, \dots, 6,$$

$$\{L_0, L_1\} = \int_V \left(\{C_1^2, C_2^2\}\rho(r,\theta,z,T)\right) rdrd\theta dz,$$

$$\{K_0, K_1\} = \int_V \left(\{C_1, C_2\}\rho(r,\theta,z,T)\right) rdrd\theta dz,$$

$$\{J_0\} = \int_V \left(\{C_1C_2\}\rho(r,\theta,z,T)\right) rdrd\theta dz.$$

4. Solution

As a powerful numerical approach, the GDQ method is hired to discretize and solve the equilibrium relations together with boundary conditions. Therefore, the *jth-order* derivatives of function $\mathscr{F}(r)$, at point (r_i, θ_j), is guessed approximately as [55]

$$\left.\frac{\partial\mathscr{F}}{\partial r}\right|_{r=r_i,\theta=\theta_j} = \sum_{m=1}^{\mathscr{N}_r}\sum_{n=1}^{\mathscr{N}_\theta} \mathscr{A}^r_{im} I^\theta_{jn} \mathscr{F}_{mn}, \tag{20a}$$

$$\left.\frac{\partial\mathscr{F}}{\partial \theta}\right|_{r=r_i,\theta=\theta_j} = \sum_{m=1}^{\mathscr{N}_r}\sum_{n=1}^{\mathscr{N}_\theta} I^r_{im} \mathscr{A}^\theta_{jn} \mathscr{F}_{mn}, \tag{20b}$$

$$\frac{\partial}{\partial r}\left(\left.\frac{\partial\mathscr{F}}{\partial \theta}\right|_{r=r_i,\theta=\theta_j}\right) = \sum_{m=1}^{\mathscr{N}_r}\sum_{n=1}^{\mathscr{N}_\theta} \mathscr{A}^r_{im} \mathscr{A}^\theta_{jn} \mathscr{F}_{mn}, \tag{20c}$$

$$\left.\frac{\partial^2\mathscr{F}}{\partial r^2}\right|_{r=r_i,\theta=\theta_j} = \sum_{m=1}^{\mathscr{N}_r}\sum_{n=1}^{\mathscr{N}_\theta} \mathscr{B}^r_{im} I^\theta_{jn} \mathscr{F}_{mn}, \tag{20d}$$

$$\left.\frac{\partial^2\mathscr{F}}{\partial \theta^2}\right|_{r=r_i,\theta=\theta_j} = \sum_{m=1}^{\mathscr{N}_r}\sum_{n=1}^{\mathscr{N}_\theta} I^r_{im} \mathscr{B}^\theta_{jn} \mathscr{F}_{mn}. \tag{20e}$$

in which $I^r_{im}\left(or\ I^\theta_{jn}\right) = \begin{cases} 1 & i = m(or\ j = n) \\ 0 & otherwise \end{cases}$.

$\mathscr{A}^r_{im}$ (or $\mathscr{A}^\theta_{jn}$) shows the weighting coefficients of the first-order derivatives in the r (or θ) direction. Also, $\mathscr{B}^r_{im}$ (or $\mathscr{B}^\theta_{jn}$) denotes the weighting coefficients of the second-order derivatives in the r (or θ) directions.

$$\mathscr{A}^r_{im} = \begin{cases} \dfrac{\xi(r_i)}{(r_i - r_m)\xi(r_m)} \ when\ i \neq m \\ -\displaystyle\sum_{k=1,k\neq i}^{\mathscr{N}_r} \mathscr{A}_{ik}\ when\ i = m \end{cases} \quad i, m = 1, 2, \dots, \mathscr{N}_r, \tag{21a}$$

$$\mathscr{A}^\theta_{jn} = \begin{cases} -\dfrac{\xi(\theta_j)}{\xi(\theta_n)(\theta_n - \theta_j)} \ when\ n \neq j \\ -\displaystyle\sum_{k=1,\ k\neq j}^{\mathscr{N}_\theta} \mathscr{A}_{jk}\ when\ n = j \end{cases} \quad n, j = 1, \dots, \mathscr{N}_\theta. \tag{21b}$$

in which

$$\xi(r_i) = \prod_{k=1,k\neq i}^{\mathscr{N}_r} (r_i - r_k), \tag{22a}$$

$$\xi(\theta_j) = \prod_{k=1,\ k\neq j}^{\mathscr{N}_\theta} (\theta_j - \theta_k). \tag{22b}$$

And

$$\mathscr{B}^r_{im} = 2\left(\mathscr{A}^r_{ii}\mathscr{A}^r_{im} - \frac{\mathscr{A}^r_{im}}{(r_i - r_m)}\right) m \neq i, m, i = 1, \dots, \mathscr{N}_r, \tag{23a}$$

$$\mathscr{B}^\theta_{jn} = 2\left(\mathscr{A}^\theta_{jj}\mathscr{A}^\theta_{jn} + \frac{\mathscr{A}^\theta_{jn}}{(\theta_n - \theta_j)}\right) n \neq j, n, j = 1, \dots, \mathscr{N}_\theta, \tag{23b}$$

$$\mathscr{B}^r_{ii} = -\sum_{k=1,k\neq i}^{\mathscr{N}_r} \mathscr{B}^r_{ik} m = i, i = 1,\ldots,\mathscr{N}_r, \tag{23c}$$

$$\mathscr{B}^\theta_{jj} = -\sum_{k=1,k\neq j}^{\mathscr{N}_\theta} \mathscr{B}^\theta_{jk}, j = 1,2,\ldots,\mathscr{N}_j, j = n. \tag{23d}$$

Here, grid-points in the r and θ directions are introduced upon the Chebyshev-Gauss-Lobatto [56]

$$r_i = \frac{R_0 + R_i}{2} - \frac{R_0 - R_i}{2}\cos\left(\frac{i-1}{\mathscr{N}_r - 1}\pi\right)\ i = 1,\ldots,\mathscr{N}_r, \tag{24a}$$

$$\theta_j = \frac{\chi}{2} - \frac{\chi}{2}\cos\left(\frac{j-1}{\mathscr{N}_\theta - 1}\pi\right). j = 1,\ldots,\ \mathscr{N}_\theta. \tag{24b}$$

Now, the discrete form of the boundary conditions and equilibrium relations is assembled in the matrix form as:

$$\left\{\begin{bmatrix} [\mathscr{M}_{dd}] & [\mathscr{M}_{db}] \\ [\mathscr{M}_{bd}] & [\mathscr{M}_{bb}] \end{bmatrix}\omega^2 + i\begin{bmatrix} [\mathscr{C}_{dd}] & [\mathscr{C}_{db}] \\ [\mathscr{C}_{bd}] & [\mathscr{C}_{bb}] \end{bmatrix}\omega + \begin{bmatrix} [\mathscr{K}_{dd}] & [\mathscr{K}_{db}] \\ [\mathscr{K}_{bd}] & [\mathscr{K}_{bb}] \end{bmatrix}\right\}\begin{Bmatrix} \Xi_d \\ \Xi_b \end{Bmatrix} = 0, \tag{25}$$

The system's characteristics, including natural frequencies along with the mode shapes, are the roots of Eq. (25). Further, the dimensionless frequency and aerodynamic pressure are defined as:

$$\{\varpi, D, \lambda\} = \left\{\omega R_o^2\sqrt{\frac{\rho_c \mathscr{A}}{D}},\ \frac{E_c h^3}{12(1-\nu_c^2)},\ \frac{\lambda_\infty R_o^3}{E_c h^3}\right\}. \tag{26}$$

At last, for numerical solution, the thermal field can be attained by replacing Eqs.)1),)20) into Eq.)10).

5. DNNs for predictive modeling

Deep neural networks (DNNs) are powerful tools for predictive modeling, particularly in complex systems like functionally graded material (FGM) sector disks, where aero-thermodynamic responses need to be accurately forecasted. These responses are critical in applications like aerospace engineering, where high temperatures and stresses demand precise material design to ensure durability and performance [57]. Using datasets generated from mathematical simulations, DNNs can be employed to model these complex interactions efficiently [58]. FGMs are composite materials where properties vary spatially to achieve desirable mechanical and thermal performance. In sector disks, FGMs can provide resistance to temperature gradients and mechanical stress by varying properties like conductivity and density. Predicting the aero-thermodynamic responses of these disks, such as temperature distribution, heat flux, and stress patterns, is crucial for optimizing their design in high-performance environments. DNNs excel in capturing nonlinear relationships and patterns in large datasets, which is essential for modeling the complex behaviors of FGMs under different conditions. The architecture of a DNN can be designed to learn the intricate patterns of aero-thermodynamic behavior by feeding it with input variables such as material composition, environmental conditions, and geometric properties of the sector disk. The network, through multiple hidden layers, can map these inputs to the aero-thermodynamic responses of interest. A common approach is to divide the dataset into training, validation, and test sets [59]. The DNN is trained on the training set to minimize prediction errors using backpropagation and gradient descent algorithms. The validation set is used to fine-tune hyperparameters like learning rate, number of layers, and neurons per layer [60]. The test set, which the model has never seen, assesses the DNN's performance in predicting the aero-thermodynamic responses of new, unseen disk configurations. The resulting model can then be used to predict how new FGM sector disks will respond under various aero-thermodynamic conditions without the need for extensive numerical simulations. This is not only computationally efficient but also provides real-time predictions for engineers working on the design and optimization of FGM disks in aerospace applications. Therefore, deep neural networks offer a robust approach to tackling the complex problem of predicting aero-thermodynamic responses, making them an invaluable tool in the field of FGM sector disk design.

5.1. Mathematical modeling of deep neural networks for predicting aero-thermodynamic responses of FGM sector disks

The mathematical modeling of deep neural networks (DNNs) for predicting the aero-thermodynamic responses of functionally graded material (FGM) sector disks relies on multiple layers of transformations and weight adjustments that map inputs (e.g., material properties, geometric features, and boundary conditions) to desired outputs (e.g., temperature distribution, thermal stresses, and displacement fields). Below is a step-by-step breakdown of the DNN mathematical model in this context:

5.1.1. Input layer (Data representation)

Let the input vector be denoted by $x \in R^n$, where $x = [x_1, x_2, \ldots, x_n]$ represents the physical parameters of the FGM sector disk such as:

- Material properties (density, thermal conductivity, etc.)
- Geometric properties (radius, thickness, etc.)
- Environmental conditions (temperature, pressure, etc.)

The dimensionality n corresponds to the number of input features relevant to the aero-thermodynamic simulation. Each input variable x_i is normalized to ensure all values are on a similar scale.

5.1.2. Hidden layers (Nonlinear transformations)

The DNN consists of multiple hidden layers, each applying a linear transformation followed by a nonlinear activation function. Let the output of the $l-th$ hidden layer be denoted as $h^{(l)} \in R^{d_l}$, where d_l is the number of neurons in layer l.

The transformation in each layer is represented as:

$$h^{(l)} = \sigma\left(W^{(l)}h^{(l-1)} + b^{(l)}\right),\ \text{for } l = 1, 2, \ldots, L. \tag{27}$$

Where:

$W^{(l)} \in R^{d_l \times d_{l-1}}$ is the weight matrix connecting layer $l-1$ to layer l.

$b^{(l)} \in R^{d_l}$ is the bias vector of layer l.

$\sigma(\cdot)$ is the activation function (typically ReLU: $\sigma(z) = max(0, z)$) that introduces nonlinearity to the model.

$h^{(l-1)}$ is the output of the previous layer or the input layer when $l = 1$.

The weights $W^{(l)}$ and biases $b^{(l)}$ are trainable parameters updated during the learning process. The number of layers L and the number of neurons per layer d_l are hyperparameters that control the capacity of the model.

5.1.3. Output layer (Aero-Thermodynamic predictions)

The final layer provides the predicted aero-thermodynamic responses. If the output consists of m different responses, the final layer produces an output vector $y \in R^m$.

The output layer is typically linear, and its transformation is given by:

$$y = W^{(L+1)}h^{(L)} + b^{(L+1)}. \tag{28}$$

Where:

$W^{(L+1)} \in R^m \times d_L$ is the weight matrix of the output layer.

$b^{(L+1)} \in R^m$ is the bias vector of the output layer.

$h^{(L)}$ is the output of the last hidden layer.

5.1.4. Loss function (Error measurement)

To train the DNN, we need to define a loss function that measures the difference between the predicted responses $\hat{y}$ and the actual responses y from the simulation dataset. For regression tasks (like predicting continuous aero-thermodynamic responses), the most common loss function is the mean squared error (MSE):

$$L(y,\ \hat{y}) = \left(\frac{1}{m}\right)\sum_{i=1}^{m}(y_i - \hat{y}_i)^2. \tag{29}$$

Where:

$y = [y_1,\ y_2,\ \dots,\ y_n]$ is the vector of true values from the dataset.
$\hat{y} = [\hat{y}_1,\ \hat{y}_2,\ \dots,\ \hat{y}_n]$ is the vector of predicted values from the DNN.
m is the number of predicted output variables (temperature, stress, displacement, etc.).

5.1.5. Optimization (training the DNN)

The goal of training is to minimize the loss function by adjusting the network's weights and biases. This is done through backpropagation and an optimization algorithm like stochastic gradient descent (SGD) or Adam. The update rule for the weights is:

$$W^{(l)} \leftarrow W^{(l)} - \eta\, \nabla_{W^{(l)}}\ L. \tag{30}$$

Where:

η is the learning rate, controlling the step size of the updates.
$\nabla_{W^{(l)}}\ L$ is the gradient of the loss with respect to the weights $W^{(l)}$.

This process continues iteratively until the loss converges to a

```
import numpy as np
import tensorflow as tf
from tensorflow.keras.models import Sequential
from tensorflow.keras.layers import Dense
from sklearn.model_selection import train_test_split
from sklearn.preprocessing import StandardScaler
# 1. Generate Example Data (you would replace this with your actual dataset)
# Simulated data: input features such as material properties, geometric properties,
environmental conditions
# Assuming 10 input features
X = np.random.rand(1000, 10)  # 1000 samples with 10 features
# Simulated outputs: aero-thermodynamic responses (e.g., temperature, stress)
# Assuming 3 outputs: temperature, stress, displacement
y = np.random.rand(1000, 3)   # 1000 samples with 3 outputs
# 2. Preprocess the Data
# Split the data into training and test sets
X_train, X_test, y_train, y_test = train_test_split(X, y, test_size=0.2, random_state=42)
# Scale the data
scaler = StandardScaler()
X_train_scaled = scaler.fit_transform(X_train)
X_test_scaled = scaler.transform(X_test)
# 3. Build the DNN Model
model = Sequential()
# Input layer (10 inputs) and first hidden layer with 64 neurons
model.add(Dense(64, input_dim=10, activation='relu'))
# Second hidden layer with 64 neurons
model.add(Dense(64, activation='relu'))
# Output layer with 3 outputs (natural frequency, displacement, and critical pressure)
model.add(Dense(3, activation='linear'))  # Linear activation for regression tasks
# 4. Compile the Model
# Loss function: Mean Squared Error (MSE) for regression tasks
# Optimizer: Adam
model.compile(optimizer='adam', loss='mean_squared_error')
# 5. Train the Model
# Training for 100 epochs with a batch size of 32
model.fit(X_train_scaled, y_train, epochs=100, batch_size=32, validation_split=0.2)
# 6. Evaluate the Model
# Evaluate the model's performance on the test set
test_loss = model.evaluate(X_test_scaled, y_test)
print(f"Test Loss (MSE): {test_loss}")
# 7. Make Predictions
# Use the trained model to predict aero-thermodynamic responses on new data
predictions = model.predict(X_test_scaled)
print("Predictions for the test set:")
print(predictions[:5])  # Display the first 5 predictions
```

Fig. 2. A Python implementation of a deep neural network using TensorFlow/Keras to predict aero-thermodynamic responses of FGM sector disks.

minimum, resulting in a trained model capable of predicting aero-thermodynamic responses.

5.1.6. Inference (prediction on new data)

Once trained, the DNN can be used to predict the aero-thermodynamic responses for new FGM sector disk configurations by inputting the relevant parameters x into the network. The output $\hat{y}$ provides the predicted responses, which can be used in the design and analysis of FGM disks in various engineering applications. Finally, Fig. 2 is a Python implementation of a deep neural network using TensorFlow/Keras to predict aero-thermodynamic responses of FGM sector disks. This DNN will take input parameters like material properties, geometric properties, and environmental conditions, and output predictions.

6. Numerical results

In this segment, firstly, convergency circumstances (Table 2) in addition to the validity of the outcomes (Table 3) are discussed. Next, after confirming the accuracy and integrity of the results, the influence of various parameters on the stability and dynamical traits of an MD-FG disk will be discussed through several plots (Figs. 3 to 10). Also, boundary conditions corresponded to Figs. 3 to 10 is SCSC.

6.1. Convergency and validation studies

To analyze and improve the accuracy of the outcomes in addition to finding the best number of nodes, that bring about accurate results, the system's first vibration frequency is listed in Table 2 for the varied number of points and boundary types. As expected, increasing the number of sample nodes in either direction leads to an increase in the precision of the outcomes. Therefore, to reach a very high accuracy for the sequent studies, it is opted as 15.

Table 3 is devoted to examining the validity and integrity of the presented problem formulation and outcomes. To this aim, the first three dimensionless vibration frequencies of an FG plate with several boundary types were derived for different values of the FG index along the z direction. From comparing the results of the current investigation with those presented in the references, it is crystal clear that the output results have quite a high accuracy, and so, it is allowable to explore the influence of several parameters on the mechanical behavior of the current system.

6.2. Benchmark results

The impacts of FG indexes, outer radius, and sector angle on the flutter instability of SCSC MD-FG disks are studied in Figs. 3 to 5. Fig. 3 displays the change of the complex vibration frequency of an MD-FG disk versus aerodynamic pressure, λ_∞, for different values of FG indexes. The outcomes of this figure disclose that the critical flutter aerodynamic pressures, i.e. λ_∞^{cr}, of the MD-FG disk moves to the left and down with escalation of the FG indexes, that is, λ_∞^{cr} corresponded to MD-FG disk reduces. In other words, increasing the FG indexes have a weakening effect on the system's stiffness.

Fig. 4 has been provided to demonstrate the influence of the outer radius, R_o, of the MD-FG disk on the complex vibration frequency of one versus aerodynamic pressure, λ_∞. From this figure, it is disclosed that the λ_∞^{cr} of the MD-FG disk moves to the right and slightly down with escalating the ratio of the outer radius to thickness, i.e. R_o/h, that is, λ_∞^{cr} corresponded to MD-FG disk decreases slightly, in a few words, increasing the R_o/h has a lessening impact on the system's stiffness.

To analyze the effect of the sector angle, θ, on the flutter boundaries of the SCSC MD-FG disk, the changes of the real and imaginary parts of the system's vibration frequency with respect to the aerodynamic pressure are plotted in Fig. 5. From Fig. 5, it is understood that the growth of the θ causes a significant reduction in the system's stiffness and both of the real and imaginary parts of the vibration frequency. Also, the λ_∞^{cr} of the MD-FG disk moves up and right by reducing the θ, that is, λ_∞^{cr} related to MD-FG disk increases.

Totally, from Figs. 3–5, compared to the R_o/h, and θ, FG indexes have a critical role to determine and shift the flutter boundaries of the system. Influence of the FG indexes, i.e. (n_r, n_θ, n_z), and outer radius, i.e. R_o, of the MD-FG disk on the change of the system's vibrational frequency, without damping effect, versus Mach number, i.e. M_∞, is analyzed in Fig. 6. To produce this figure, it is presumed that $R_i = 0$, $T_b = 300$, $T_t = 330$, $\theta = \frac{\pi}{4}$, $\lambda_\infty = 100$, $\theta_\infty = 0$, and $\mathscr{u}_\infty = 300$. The outcomes of Fig. 6 disclose that the supersonic airflow characteristic of the MD-FG disk weakens with intensifying the values of FG indexes in varied directions, and the vibration frequency of the system decreases, that is, increasing the FG indexes causes shifting the Mach number corresponding to the flutter boundaries, i.e. M_∞^{cr}, to the left and down. Also, increasing the R_o/h leads to a slight change in the ϖ, but it can lead to the escalation of the M_∞^{cr}.

The impact of the sector angle, θ, and temperature change, ΔT, on the variation of the system's vibrational frequency versus Mach number, M_∞, is illustrated in Fig. 7. Also, the constant parameters corresponding to this figure is $R_i = 0$, $R_o = 50h$, $\lambda_\infty = 100$, $\theta_\infty = 0$, $\mathscr{u}_\infty = 300$, and $(n_r, n_\theta, n_z) = (0.5, 0.5, 0.5)$. From the current plot, it is concluded that increasing the θ or ΔT has a decreasing effect on the ϖ, that is, these parameters have a weakening impact on the system's stiffness. Additionally, increasing the θ or ΔT leads to moderate and move the M_∞^{cr} to the left and down.

Totally, upon the Figs. 6 and 7, the impacts of the R_o/h, and FG indexes on the M_∞^{cr} and flutter boundaries of the system are more remarkable compared to the effect of θ, and ΔT on those. In Figs. 8–10, separately, the influence of parameters such as sector angle, i.e. θ, Mach number, i.e. M_∞, in addition to aerodynamic pressure, i.e. λ_∞, on the variation of the dimensionless frequency, i.e. ϖ, of an SCSC MD-FG disk with respect to the air yaw angle, i.e. θ_∞, is investigated. Upon the Fig. 7, lessening the values of the θ lead to an amazing escalation in the system's ϖ . Also, according to Fig. 9 (and Fig. 10), as a result of heightening the M_∞ (and λ_∞), the vibrational frequency of the MD-FG disk increases. Generally, from Figs. 8–10, it is seen that growth of the θ_∞ has an increase/decrease influence on the ϖ, and also the maximum value of the ϖ, i.e. ϖ_{max}, could happen at the $\theta_\infty \cong 100$. Moreover, varying the parameters θ, M_∞, and λ_∞ has not had a considerable impact on the θ_∞ corresponded to the ϖ_{max}. Finally, compared to the M_∞, and λ_∞, θ has a critical impact on the ϖ, i.e. $\theta > M_\infty > \lambda_\infty$.

Fig. 11 shows the mode shape of the presented sector annular plate for various. λ_∞ values. As is seen, by increasing the λ_∞ parameter, the maximum sector annular plate's deflection value increases. Also, by increasing the λ_∞ parameter, more deformation can be seen at the outer radius than at the middle surface. As well as this, as an interesting result for related industries, by increasing the λ_∞ parameter, the continuous deformation can be seen at the outer radius than the inner one.

6.3. The results of the presented DNN

To predict the aero-thermodynamic responses of Functionally Graded Material (FGM) sector disks, a Deep Neural Network (DNN)

Table 2
Variation of the system's first vibration frequency (ϖ) against the number of nodes with $R_i = 0$, $\frac{R_o}{h} = 50$, $T_b = 300$, $T_t = 310$, $\theta = \frac{\pi}{4}$, $\lambda_\infty = 1$, $\mathscr{M}_\infty = \sqrt{2}$, $\theta_\infty = 0$, $\mathscr{u}_\infty = 300$, and $n_r = n_\theta = n_z = 0.5$.

Boundary condition's	$(\mathscr{N}_r, \mathscr{N}_\theta)$				
	(7,7)	(9,9)	(11,11)	(13,13)	(15,15)
HSSS	30.7512	26.6132	26.5096	26.5096	26.5096
HSCS	36.3112	33.7123	33.6007	33.6007	33.6007
HSFS	11.5231	9.8142	9.7106	9.7106	9.7106

Table 3
Comparison of dimensionless frequency for an FG plate made of Aluminum and Alumina [61].

		SCS			SSS			SFS		
		Mode								
n_z		1	2	3	1	2	3	1	2	3
1	Present	8.4962	33.0851	74.1261	4.1039	24.7230	61.6900	7.4841	31.9801	73.0001
	Ref. [62]	8.4988	33.0865	74.1277	4.1057	24.7247	61.6921	7.4899	31.9818	73.0014
	Ref. [63]	8.4988	33.0865	74.1277	4.1057	24.7247	61.6921	–	–	–
	Ref. [64]	8.498	33.086	74.127	4.105	24.724	61.692	7.489	31.981	73.001
	Ref. [65]	8.500	33.093	–	4.106	24.742	–	7.491	31.255	–
2	Present	8.1212	31.6232	70.8521	3.9227	23.6301	58.9673	7.1572	30.5631	69.7756
	Ref. [62]	8.1236	31.6258	70.8551	3.9244	23.6332	58.9685	7.1592	30.5698	69.7785
	Ref. [63]	8.1236	31.6258	70.8551	3.9244	23.6332	58.9685	–	–	–
	Ref. [64]	8.123	31.625	70.855	3.924	23.633	58.968	7.159	30.569	69.778
	Ref. [65]	8.125	31.634	–	3.925	23.651	–	7.161	29.877	–
3	Present	7.9091	30.7952	69.0000	3.8194	23.0101	57.4226	6.9701	29.7672	67.9472
	Ref. [62]	7.9112	30.7988	69.0024	3.8218	23.0152	57.4266	6.972	29.7705	67.9539
	Ref. [63]	7.9112	30.7988	69.0024	3.8218	23.0152	57.4266	–	–	–
	Ref. [64]	7.911	30.798	69.002	3.821	23.015	57.426	6.972	29.7705	67.954
4	Present	7.7302	30.1041	67.45112	3.7326	22.4958	56.1321	6.8132	29.1003	66.4251
	Ref. [62]	7.7335	30.1074	67.4532	3.7360	22.4985	56.1372	6.8155	29.1021	66.4282
	Ref. [63]	7.7335	30.1074	67.4532	3.736	22.4985	56.1370	–	–	–
	Ref. [64]	7.733	30.107	67.453	3.736	22.498	56.137	6.815	29.102	66.428
5	Present	7.5682	29.4814	66.0563	3.6552	22.0294	54.9699	6.6732	28.4942	65.0492
	Ref. [62]	7.5738	29.4854	66.0598	3.6588	22.0338	54.9777	6.6747	28.5009	65.0561
	Ref. [63]	7.5738	29.4854	66.0598	3.6588	22.0338	54.9777	–	–	–
	Ref. [64]	7.573	29.485	66.059	3.658	22.033	54.977	6.674	28.501	65.056
	Ref. [65]	7.576	29.496	–	3.659	22.052	–	6.677	27.857	–

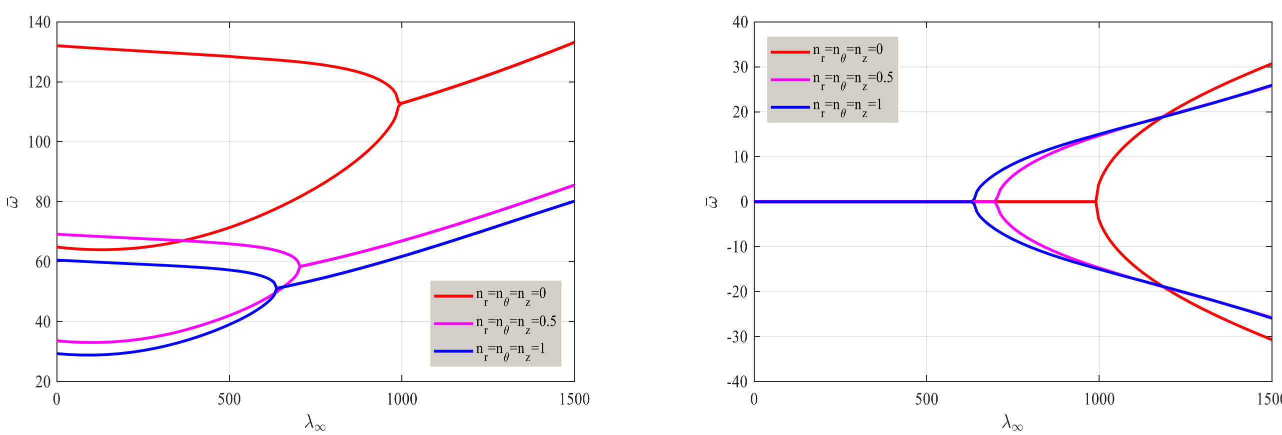

Fig. 3. The change of real and imaginary parts of eigenvalue for the MD-FG disk versus the aerodynamic pressure under varied FG indexes with $R_i = 0$, $R_o = 50h$, $T_b = 300$, $T_t = 330$, $\theta = \frac{\pi}{4}$, $M_\infty = \sqrt{2}$, $\theta_\infty = 0$, and $\varkappa_\infty = 300$.

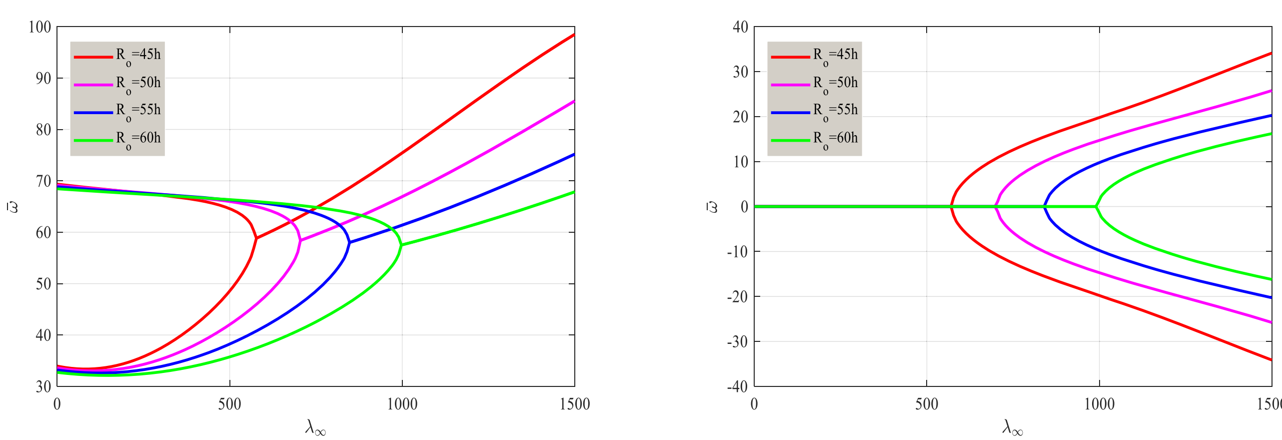

Fig. 4. The change of real and imaginary parts of eigenvalue for the MD-FG disk versus the aerodynamic pressure under varied outer radius with $R_i = 0$, $T_b = 300$, $T_t = 330$, $\theta = \frac{\pi}{4}$, $M_\infty = \sqrt{2}$, $\theta_\infty = 0$, $\varkappa_\infty = 300$, and $(n_r,\ n_\theta,\ n_z) = (0.5, 0.5, 0.5)$.

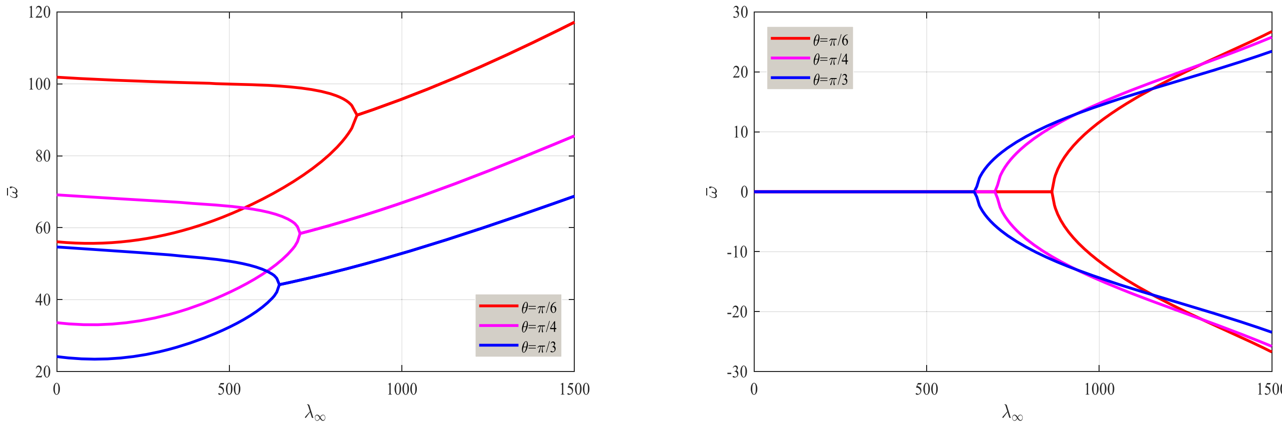

Fig. 5. The change of real and imaginary parts of eigenvalue for the MD-FG disk versus the aerodynamic pressure under varied sector angles with $R_i = 0$, $R_o = 50h$, $T_b = 300$, $T_t = 330$, $M_\infty = \sqrt{2}$, $\theta_\infty = 0$, $\mathscr{u}_\infty = 300$, and $(n_r, n_\theta, n_z) = (0.5, 0.5, 0.5)$.

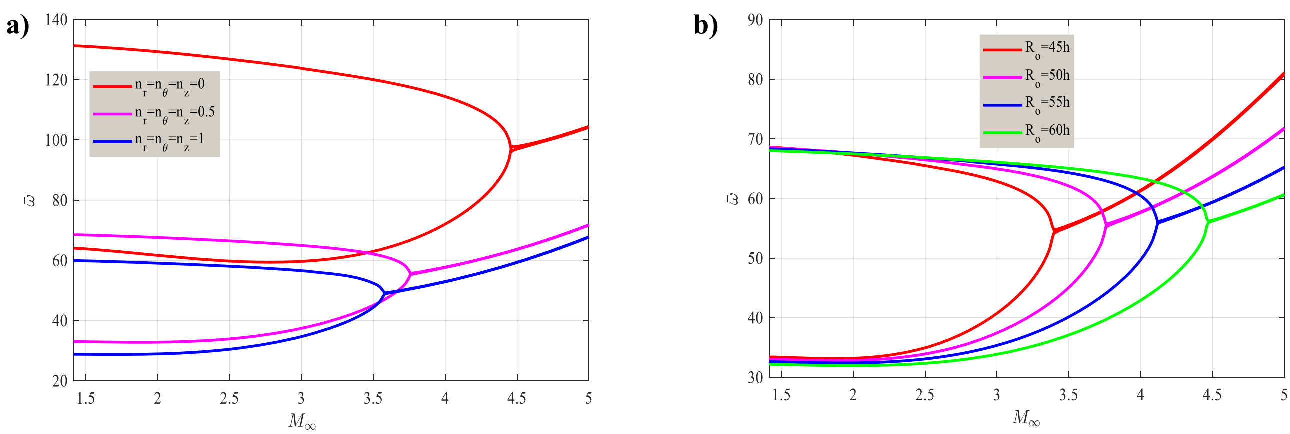

Fig. 6. On the airflow dynamics of an MD-FG disk with several values of a) FG indexes and $R_o = 50h$ b) outer radius and $(n_r, n_\theta, n_z) = (0.5, 0.5, 0.5)$, in addition to regarding the impact of M_∞.

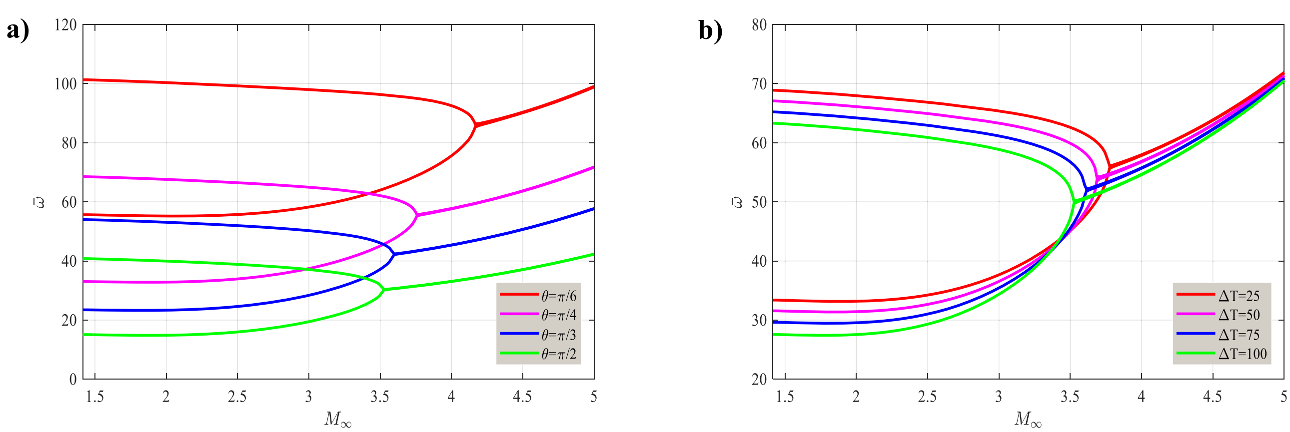

Fig. 7. On the airflow dynamics of an MD-FG disk with several values of a) sector angle and $T_b = 300$, $T_t = 330$ b) temperature difference and $\theta = \frac{\pi}{4}$, in addition to regarding the impact of M_∞.

model can be developed using datasets from mathematical simulations. These datasets include key input features like material properties (e.g., thermal conductivity, density), geometric properties (e.g., thickness, radius), and environmental conditions (e.g., temperature, and pressure). The outputs of the DNN represent aero-thermodynamic responses such as natural frequency, flutter load, and displacement fields. The DNN model consists of multiple hidden layers, with each layer applying nonlinear transformations to learn complex relationships between input and output data. The model is trained using a regression approach, minimizing the Mean Squared Error (MSE) between predicted and actual values. The trained DNN can then be used for fast, accurate predictions of aero-thermodynamic responses under varying conditions, making it suitable for optimizing FGM disk design in aerospace applications. Fig. 12 depicts the training and validation performance of a DNN model over 300 epochs, as represented by the Mean Squared Error (MSE) on a logarithmic scale. The MSE is a common loss function used in

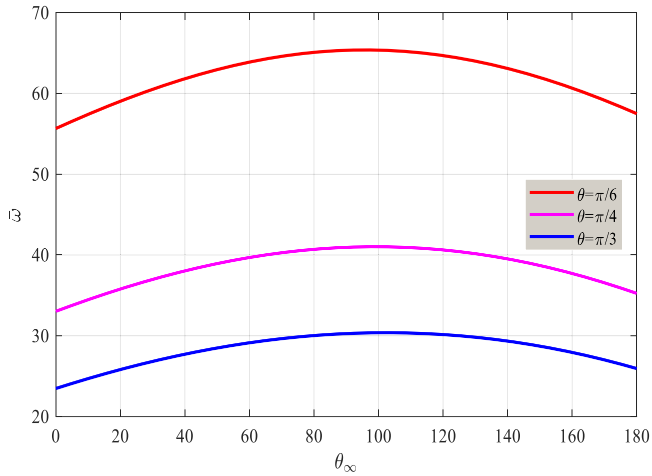

Fig. 8. Frequency of an MD-FG disk with $R_i = 0$, $R_o = 50h$, $T_b = 300$, $T_t = 330$, $\lambda_\infty = 100$, $M_\infty = \sqrt{2}$, $u_\infty = 300$, and $(n_r,\ n_\theta,\ n_z) = (0.5, 0.5, 0.5)$ in addition to regarding the impact of θ_∞.

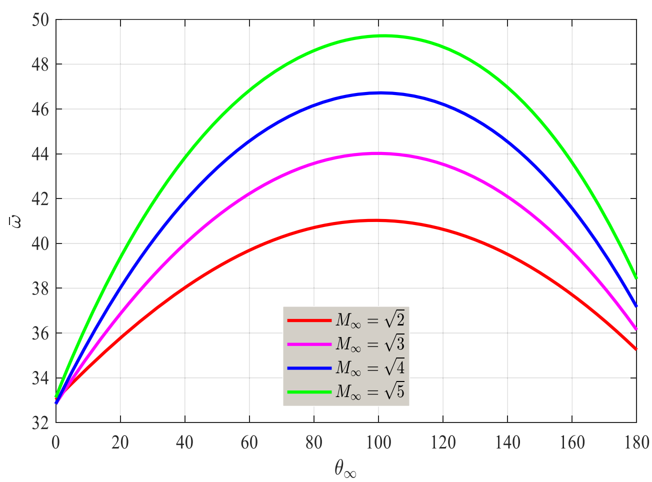

Fig. 9. Frequency of an MD-FG disk with $R_i = 0$, $R_o = 50h$, $T_b = 300$, $T_t = 330$, $\lambda_\infty = 100$, $\theta = \frac{\pi}{4}$, $u_\infty = 300$, and $(n_r,\ n_\theta,\ n_z) = (0.5, 0.5, 0.5)$ in addition to regarding the impact of θ_∞.

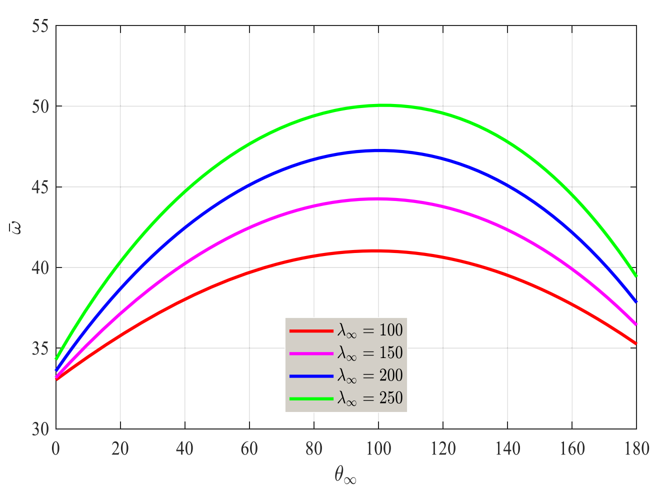

Fig. 10. Frequency of an MD-FG disk with $R_i = 0$, $R_o = 50h$, $T_b = 300$, $T_t = 330$, $\theta = \frac{\pi}{4}$, $M_\infty = \sqrt{2}$, $u_\infty = 300$, and $(n_r,\ n_\theta,\ n_z) = (0.5, 0.5, 0.5)$ in addition to regarding the impact of θ_∞.

regression tasks to evaluate the average squared difference between predicted and actual values. In the plot, the red curve represents the MSE of the training data, while the blue curve shows the MSE for the validation data. Initially, both training and validation MSE are relatively high, with values around 10°, indicating significant errors in the early stages of training. However, both curves drop sharply during the first 50 epochs, demonstrating rapid improvement in the model's performance as it learns to minimize the error. After around 50 epochs, the training curve begins to fluctuate slightly but maintains a steady downward trend, reaching a low value around 10^{-2} to 10^{-3}. This indicates that the model continues to learn and improve on the training data, though with diminishing returns. The validation curve also follows a similar trend, indicating that the model is generalizing well to unseen data and is not overfitting significantly. However, the slight gap between the training and validation errors shows that there is some variance in the model's ability to generalize, which could be improved with additional regularization techniques. Overall, this figure suggests that the DNN model is well-trained, with both training and validation errors converging to a low value, confirming the model's suitability for predicting the aero-thermodynamic responses of FG sector disks.

This section examines the effects of R^2 and RMSE on the results shown in Tables 4 and 5. It has been noted that responses with higher RMSE and R^2 values are more accurate. It is thus recommended to choose R^2=0.9921, RMSE=0.3896, and 789 samples when selecting the findings. The results of the mathematical modeling are also shown using MS (mathematics simulation).

Tables 4 and 5 show how the weight percentage of n_z affect the dimensionless frequency of the present structure. The part that follows will go into more information on this subject.

After testing, training, and validating the results, the following parameters should be used to correctly predict aero-thermodynamic responses of FGM sector disks.

Parameter	Value/Details
Number of Input Features	10 (material, geometric, and environmental properties)
Number of Hidden Layers	2 hidden layers
Neurons per Layer	64 neurons per hidden layer
Activation Function	ReLU for hidden layers, Linear for output layer
Loss Function	Mean Squared Error (MSE)
Optimizer	Adam
Learning Rate	Default (Adam automatically adjusts it)
Batch Size	32
Epochs	250
RMSE	0.3896
R^2	0.9921

7. Conclusion

Composite sector disks play a pivotal role in enhancing the performance, efficiency, and safety of aerospace structures and systems exposed to supersonic airflow and thermal environments. Their integration into aerospace design allows for the development of advanced, resilient, and lightweight solutions tailored to the demanding conditions of aerospace applications. Vibrational characteristics of an MD-FG sector disk was studied based on the Q3D-NRT along with the refined zigzag hypothesis. The equilibrium equations along with the associated boundary conditions were obtained by exploiting Hamilton's principle. The solution method was established based on GDQ approach for various boundary types, after attaining the effective material properties. After obtaining the mathematics results, appropriate datasets are made for testing, training, and validation of the deep neural networks technique. An exhaustive parametric investigation was provided to study the role of free stream speed, temperature changes, air yaw angle, aerodynamic pressure, boundary domains, and Mach number on the flutter boundaries and vibrational traits of the MD-FG sector disk. Some highlights of this paper can be expressed in a few words as:

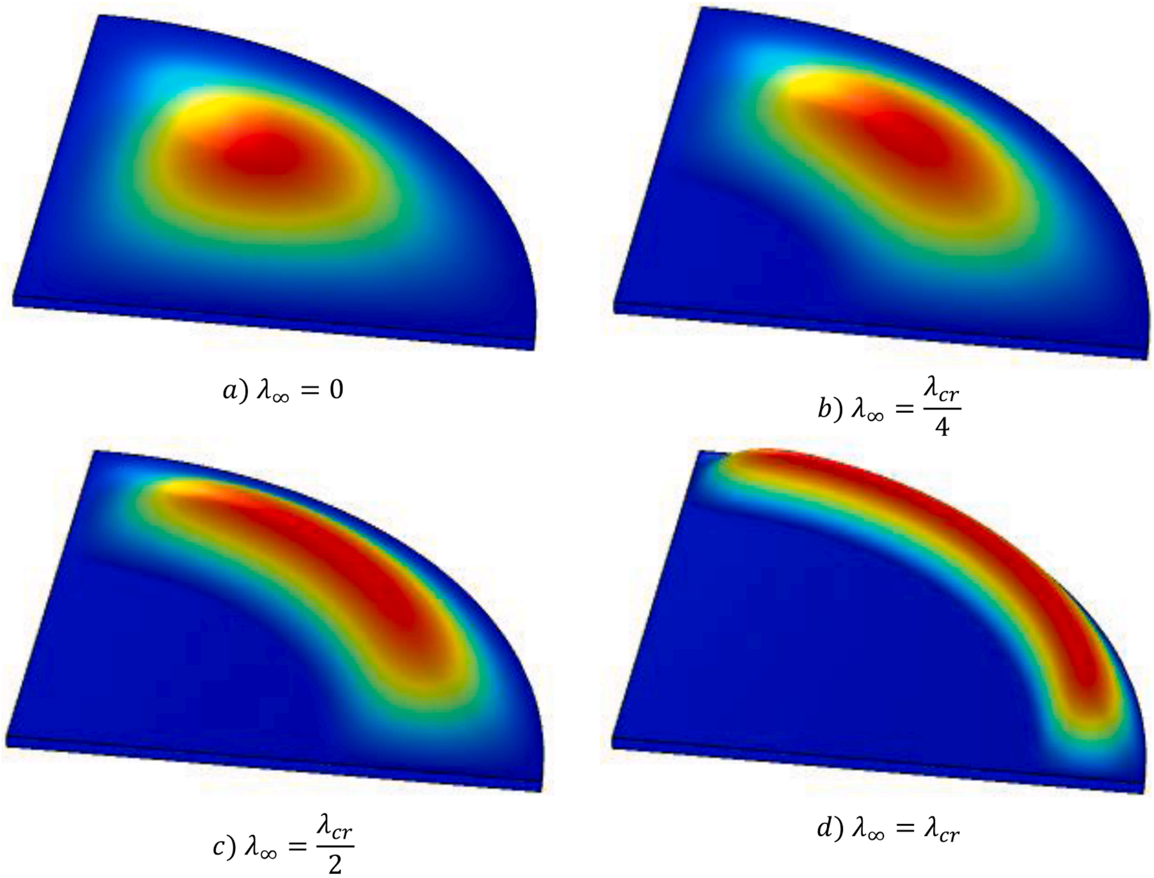

Fig. 11. The mode shape of the presented sector annular plate for various λ_∞ values.

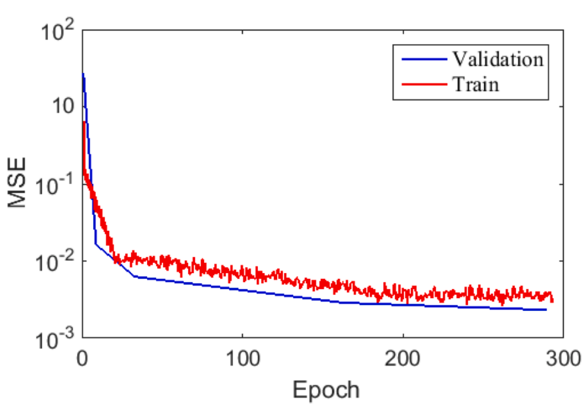

Fig. 12. Performance of the DNN model.

Table 4
Dimensionless frequency of the DNN model for different RMSE and n_z values.

	MS	Predicted		
		$RMSE_{Train} = 0.2861$	$RMSE_{Train} = 0.3152$	$RMSE_{Train} = 0.3896$
1	8.4962	6.966884	8.156352	8.411238
2	8.1212	6.659384	7.796352	8.039988
3	7.9091	6.485462	7.592736	7.830009
4	7.7302	6.338764	7.420992	7.652898
5	7.5682	6.205924	7.265472	7.492518

Table 5
Performance of the DNN model for dimensionless frequency for various R^2 and n_z values.

	MS	Predicted		
		R^2=0.9151	R^2=0.9563	R^2=0.9921
1	8.4962	7.476656	8.07139	8.453719
2	8.1212	7.146656	7.71514	8.080594
3	7.9091	6.960008	7.513645	7.869555
4	7.7302	6.802576	7.34369	7.691549
5	7.5682	6.660016	7.18979	7.530359

- v In addition to the real part and imaginary part of the $\overline{\omega}$, the λ_∞^{cr} of the MD-FG disk, which is related to the flutter boundary, could reduce with the growth of the FG indexes, R_o/h, or θ, that is, increasing each of these parameters has a lessening impact on the system's stiffness.
- v Against of the R_o/h, increasing the FG indexes, θ, or ΔT leads to the reduction of the M_∞^{cr}, that is, these parameters have a weakening impact on the system's stiffness.
- v The result of intensifying the M_∞, or λ_∞ is escalation of the system's $\overline{\omega}$. Apart from, escalating the θ_∞ leads to an increase/decrease in behavior in the $\overline{\omega}$.
- v Compared to the M_∞, and λ_∞, θ has a chief role in the $\overline{\omega}$, i. e. $\theta > M_\infty > \lambda_\infty$.
- v Changing the θ, M_∞, and λ_∞ has a minor effect on the θ_∞ related to the $\overline{\omega}_{max}$. Also, θ_∞^{max} in which $\overline{\omega} = \overline{\omega}_{max}$ is equal to 100.

CRediT authorship contribution statement

Shaoyong Han: Formal analysis, Investigation, Methodology, Resources, Software, Writing – review & editing. **Zhen Wang:** Writing –

review & editing, Writing – original draft, Visualization, Validation, Supervision, Software, Resources, Investigation. **Mohammed El-Meligy:** Resources, Software, Validation, Visualization, Writing – review & editing. **Kashif Saleem:** Investigation, Software, Validation, Writing – review & editing.

Declaration of competing interest

The authors declare that they have no conflict of interest.

Data availability

Data will be made available on request.

Acknowledgement

The authors extend their appreciation to King Saud University for funding this work through Researchers Supporting Project number (RSPD2024R697), King Saud University, Riyadh, Saudi Arabia.

References

[1] M. Chitour, et al., Stability analysis of imperfect FG sandwich plates containing metallic foam cores under various boundary conditions, in: Structures, 61, Elsevier, 2024 106021, 2024.
[2] D.E. Lafi, et al., Combined influence of variable distribution models and boundary conditions on the thermodynamic behavior of FG sandwich plates lying on various elastic foundations, Struct. Eng. Mech. 89 (2) (2024) 103, 2024.
[3] A. Tounsi, et al., Influences of different boundary conditions and hygro-thermal environment on the free vibration responses of FGM sandwich plates resting on viscoelastic foundation, Int. J. Struct. Stab. Dyn. (2023) 2450117, 2023.
[4] A. Tounsi, et al., Free vibration investigation of functionally graded plates with temperaturedependent properties resting on a viscoelastic foundation, Struct. Eng. Mech., An Int'l Journal 86 (1) (2023) 1–16, 2023.
[5] A. Tounsi, et al., Thermodynamical bending analysis of P-FG sandwich plates resting on nonlinear visco-Pasternak's elastic foundations, Steel Compos. Struct. 49 (3) (2023) 307–323, 2023.
[6] F. Bourada, et al., An integral quasi-3D computational model for the hygro-thermal wave propagation of imperfect FGM sandwich plates, Comput. Concr. 32 (1) (2023) 61–74.
[7] I.M. Mudhaffar, A. Chikh, A. Tounsi, M.A. Al-Osta, M.M. Al-Zahrani, S.U. Al-Dulaijan, Impact of viscoelastic foundation on bending behavior of FG plate subjected to hygro-thermo-mechanical loads, Struct. Eng. Mech., An Int'l Journal 86 (2) (2023) 167–180, 2023.
[8] Ö. Civalek, M. Avcar, Free vibration and buckling analyses of CNT reinforced laminated non-rectangular plates by discrete singular convolution method, Eng. Comput. 38 (Suppl 1) (2022) 489–521.
[9] O. Ragb, M. Mohamed, M.S. Matbuly, O. Civalek, Sinc and discrete singular convolution for analysis of three-layer composite of perovskite solar cell, Int. J. Energy Res. 46 (4) (2022) 4279–4300.
[10] I. Barbaros, Y. Yang, B. Safaei, Z. Yang, Z. Qin, M. Asmael, State-of-the-art review of fabrication, application, and mechanical properties of functionally graded porous nanocomposite materials, Nanotechnol. Rev. 11 (1) (2022) 321–371.
[11] M.W. Zaitoun, et al., An efficient computational model for vibration behavior of a functionally graded sandwich plate in a hygrothermal environment with viscoelastic foundation effects, Eng. Comput. 39 (2) (2023) 1127–1141, 2023.
[12] M.W. Zaitoun, et al., Influence of the visco-Pasternak foundation parameters on the buckling behavior of a sandwich functional graded ceramic–metal plate in a hygrothermal environment, Thin-Walled Structures 170 (2022) 108549, 2022.
[13] K. Bouafia, et al., Bending and free vibration characteristics of various compositions of FG plates on elastic foundation via quasi 3D HSDT model, Steel Compos. Struct. Int. J. 41 (4) (2021) 487–503, 2021.
[14] D. Kouider, et al., An original four-variable quasi-3D shear deformation theory for the static and free vibration analysis of new type of sandwich plates with both FG face sheets and FGM hard core, Steel Compos. Struct. Int. J. 41 (2) (2021) 167–191, 2021.
[15] M.A. Al-Osta, et al., Influence of porosity on the hygro-thermo-mechanical bending response of an AFG ceramic-metal plates using an integral plate model, Smart Struct. Syst. Int. J. 28 (4) (2021) 499–513.
[16] A. Memarzadeh, E.C. Onyibo, M. Asmael, B. Safaei, Dynamic effect of ply angle and fiber orientation on composite plates, Spectr. Mech. Eng. Oper. Res. 1 (1) (2024) 90–110.
[17] B. Safaei, N. Ahmed, A. Fattahi, Free vibration analysis of polyethylene/CNT plates, Eur. Phys. J. Plus 134 (6) (2019) 271.
[18] A. Fattahi, The application of nonlocal elasticity to determine vibrational behavior of FG nanoplates, Steel Compos. Struct. Int. J. 32 (2) (2019) 281–292.
[19] H.-S. Shen, Functionally Graded materials: Nonlinear Analysis of Plates and Shells, CRC press, 2016.
[20] M. Javani, M.R. Eslami, Y. Kiani, Active control of thermally induced vibrations of temperature-dependent FGM circular plate with piezoelectric sensor/actuator layers, Aerosp. Sci. Technol. 146 (2024) 108997, https://doi.org/10.1016/j.ast.2024.108997, 2024/03/01/.
[21] R. Mohammadi, M. Hosseini, Modeling and free vibration analysis of a rotating functionally graded thin-walled hub-blade system under aerothermoelastic loading, Aerosp. Sci. Technol. 146 (2024) 108935, https://doi.org/10.1016/j.ast.2024.108935, 2024/03/01/.
[22] K. Xie, H. Chen, Y. Wang, J. Li, F. Jin, Nonlinear dynamic analysis of a geometrically imperfect sandwich beam with functionally graded material facets and auxetic honeycomb core in thermal environment, Aerosp. Sci. Technol. 144 (2024) 108794, https://doi.org/10.1016/j.ast.2023.108794, 2024/01/01/.
[23] A. Fattahi, B. Safaei, N. Ahmed, A comparison for the non-classical plate model based on axial buckling of single-layered graphene sheets, The European Physical Journal Plus 134 (11) (2019) 555.
[24] B. Safaei, A. Fattahi, Free vibrational response of single-layered graphene sheets embedded in an elastic matrix using different nonlocal plate models, Mechanics 23 (5) (2017) 678–687.
[25] P. Ghanati, B. Safaei, Elastic buckling analysis of polygonal thin sheets under compression, Indian Journal of Physics 93 (1) (2019) 47–52, 2019.
[26] S. Zhao, X. Zhang, S. Zhang, B. Safaei, Z. Qin, F. Chu, A unified modeling approach for rotating flexible shaft-disk systems with general boundary and coupling conditions, Int. J. Mech. Sci. 218 (2022) 107073.
[27] M. Babaei, M.H. Hajmohammad, K. Asemi, Natural frequency and dynamic analyses of functionally graded saturated porous annular sector plate and cylindrical panel based on 3D elasticity, Aerosp. Sci. Technol. 96 (2020) 105524.
[28] M. Khorasani, Z. Soleimani-Javid, E. Arshid, L. Lampani, Ö. Civalek, Thermo-elastic buckling of honeycomb micro plates integrated with FG-GNPs reinforced Epoxy skins with stretching effect, Compos. Struct. 258 (2021) 113430, 2021.
[29] K. Mercan, A.K. Baltacıoglu, Ö. Civalek, Free vibration of laminated and FGM/CNT composites annular thick plates with shear deformation by discrete singular convolution method, Compos. Struct. 186 (2018) 139–153, 2018.
[30] E. Sobhani, A.R. Masoodi, O. Civalek, A.R. Ahmadi-Pari, Agglomerated impact of CNT vs. GNP nanofillers on hybridization of polymer matrix for vibration of coupled hemispherical-conical-conical shells, Aerosp. Sci. Technol. 120 (2022) 107257, 2022.
[31] E. Sobhani, A. Arbabian, Ö. Civalek, M. Avcar, The free vibration analysis of hybrid porous nanocomposite joined hemispherical–cylindrical–conical shells, Eng. Comput. (2021) 1–28, 2021.
[32] J. Tang, S. Wu, M. Habibi, M. Safarpour, H.E. Ali, Flutter analysis of multi-directional functionally graded sector poroelastic disks, Aerosp. Sci. Technol. 140 (2023) 108481.
[33] B. Uzun, M.Ö. Yaylı, Ö. Civalek, An investigation on static, vibration and stability analyses of elastically restrained FG porous Timoshenko nanobeams, Microsystem Technologies (2024) 1–23.
[34] A.E. Abouelregal, Ö. Civalek, B. Akgöz, A Size-Dependent Non-Fourier Heat Conduction Model for Magneto-Thermoelastic Vibration Response of Nanosystems, Journal of Applied and Computational Mechanics (2024).
[35] M.A. Steinberg, Materials for aerospace, Sci. Am. 255 (4) (1986) 66–73.
[36] M. Şimşek, Bi-directional functionally graded materials (BDFGMs) for free and forced vibration of Timoshenko beams with various boundary conditions, Compos. Struct. 133 (2015) 968–978.
[37] M. Esmaeilzadeh, M. Golmakani, Y. Luo, M. Bodaghi, Transient behavior of imperfect bi-directional functionally graded sandwich plates under moving loads, Eng. Comput. (2021) 1–11.
[38] F. Allahkarami, H. Tohidi, R. Dimitri, F. Tornabene, Dynamic stability of bi-directional functionally graded porous cylindrical shells embedded in an elastic foundation, Applied Sciences 10 (4) (2020) 1345.
[39] S. Hashemi, A.A. Jafari, Nonlinear free and forced vibrations of in-plane bi-directional functionally graded rectangular plate with temperature-dependent properties, Int. J. Struct. Stab. Dyn. 20 (08) (2020) 2050097.
[40] R. Saini, R. Lal, Axisymmetric vibrations of temperature-dependent functionally graded moderately thick circular plates with two-dimensional material and temperature distribution, Eng. Comput. (2020) 1–16.
[41] H.H. Patil, J. Pitchaimani, Sound radiation characteristics of a beam under supersonic airflow and non-uniform temperature field, Aerosp. Sci. Technol. 147 (2024) 109001, https://doi.org/10.1016/j.ast.2024.109001, 2024/04/01/.
[42] Z. Song, Y. Chen, Z. Li, J. Sha, F. Li, Axially functionally graded beams and panels in supersonic airflow and their excellent capability for passive flutter suppression, Aerosp. Sci. Technol. 92 (2019) 668–675, https://doi.org/10.1016/j.ast.2019.06.042, 2019/09/01/.
[43] Y. Chai, Z. Song, F. Li, Investigations on the aerothermoelastic properties of composite laminated cylindrical shells with elastic boundaries in supersonic airflow based on the Rayleigh–Ritz method, Aerosp. Sci. Technol. 82-83 (2018) 534–544, https://doi.org/10.1016/j.ast.2018.09.040, 2018/11/01/.
[44] M. Eshaghi, The effect of magnetorheological fluid and aerodynamic damping on the flutter boundaries of MR fluid sandwich plates in supersonic airflow, European Journal of Mechanics-A/Solids 82 (2020) 103997.
[45] R. Zhong, B. Qin, Q. Wang, W. Shao, C. Shuai, Investigation on flutter instability of magnetic-electric-thermo-elastic functionally graded plates in the supersonic airflow with any yawed angle, Int. J. Mech. Sci. 198 (2021) 106356.
[46] X. Zhou, Y. Wang, W. Zhang, Vibration and flutter characteristics of GPL-reinforced functionally graded porous cylindrical panels subjected to supersonic flow, Acta Astronaut. 183 (2021) 89–100.

[47] H. Asadi, Q. Wang, Dynamic stability analysis of a pressurized FG-CNTRC cylindrical shell interacting with supersonic airflow, Composites Part B: Engineering 118 (2017) 15–25.

[48] V. Khalafi, J. Fazilati, Panel flutter analysis of cracked functionally graded plates in yawed supersonic flow with thermal effects, Appl Math Model 101 (2022) 259–275.

[49] J. Reddy, C. Chin, Thermomechanical analysis of functionally graded cylinders and plates, Journal of thermal Stresses 21 (6) (1998) 593–626.

[50] R. Barretta, L. Feo, R. Luciano, F.M. de Sciarra, R. Penna, Functionally graded Timoshenko nanobeams: a novel nonlocal gradient formulation, Composites Part B: Engineering 100 (2016) 208–219.

[51] R.B. Hetnarski, M.R. Eslami, G. Gladwell, Thermal stresses: Advanced Theory and Applications, Springer, 2009.

[52] R. Aboutalebi, Three-dimensional flutter analysis of a novel circular sandwich plate employing hyperbolic shear deformation theory, Aerosp. Sci. Technol. 150 (2024) 109223, https://doi.org/10.1016/j.ast.2024.109223, 2024/07/01/.

[53] Q. Dai, C. Zheng, Y. Liu, Q. Han, Z. Qin, F. Chu, Dynamic modeling and parametric instability analysis of internally damped rotating composite shafts in inertial and rotating frames, Aerosp. Sci. Technol. (2024) 109253, https://doi.org/10.1016/j.ast.2024.109253, 2024/05/27/.

[54] T. Fu, X. Wang, T. Rabczuk, Broadband low-frequency sound insulation of stiffened sandwich PFGM doubly-curved shells with positive, negative and zero Poisson's ratio cellular cores, Aerosp. Sci. Technol. 147 (2024) 109049, https://doi.org/10.1016/j.ast.2024.109049, 2024/04/01/.

[55] C. Shu, Differential Quadrature and Its Application in Engineering, Springer Science & Business Media, 2012.

[56] F. Tornabene, N. Fantuzzi, F. Ubertini, E. Viola, Strong formulation finite element method based on differential quadrature: a survey, Appl. Mech. Rev. 67 (2) (2015), https://doi.org/10.1115/1.4028859.

[57] E. Samaniego, et al., An energy approach to the solution of partial differential equations in computational mechanics via machine learning: concepts, implementation and applications, Comput. Methods Appl. Mech. Eng. 362 (2020) 112790, 2020.

[58] X. Zhuang, H. Guo, N. Alajlan, H. Zhu, T. Rabczuk, Deep autoencoder based energy method for the bending, vibration, and buckling analysis of Kirchhoff plates with transfer learning, European Journal of Mechanics-A/Solids 87 (2021) 104225, 2021.

[59] A. Mishra, C. Anitescu, P.R. Budarapu, S. Natarajan, P.R. Vundavilli, T. Rabczuk, An artificial neural network based deep collocation method for the solution of transient linear and nonlinear partial differential equations, Frontiers of Structural and Civil Engineering 18 (8) (2024) 1296–1310.

[60] Y. Wang et al., "Kolmogorov Arnold Informed neural network: a physics-informed deep learning framework for solving PDEs based on Kolmogorov Arnold Networks," *arXiv preprint* arXiv:2406.11045, 2024.

[61] H. Bagheri, Y. Kiani, M. Eslami, Asymmetric thermo-inertial buckling of annular plates, Acta Mech. 228 (4) (2017) 1493–1509.

[62] R. Lal, R. Saini, Vibration analysis of FGM circular plates under non-linear temperature variation using generalized differential quadrature rule, Applied Acoustics 158 (2020) 107027.

[63] R. Lal, N. Ahlawat, Axisymmetric vibrations and buckling analysis of functionally graded circular plates via differential transform method, European Journal of Mechanics-A/Solids 52 (2015) 85–94.

[64] K.K. Żur, Quasi-Green's function approach to free vibration analysis of elastically supported functionally graded circular plates, Compos. Struct. 183 (2018) 600–610.

[65] T. Wu, Y. Wang, G. Liu, Free vibration analysis of circular plates using generalized differential quadrature rule, Comput. Methods Appl. Mech. Eng. 191 (46) (2002) 5365–5380.